physica status solidi rrl
www.pss-rapid.com

Effects of Y Dopant on Lattice Distortion and Electrical Properties of In_3SbTe_2 Phase-Change Material

Minho Choi, Heechae Choi, Sehyun Kwon, Seungchul Kim, Kwang-Ryeol Lee, Jinho Ahn,* and Yong Tae Kim**

Using a computational high-throughput screening method, 29 doping elements have been investigated for improving the thermal and electrical characteristics of In_3SbTe_2 (IST) phase-change material. Among the 29 dopants, it is found that Y offers largest distortion in the lattice structure of IST with negative doping formation energy while Y substitutes the In site. The atomic lattice images clearly show that the In site is substituted by Y and the distortion angles of the Y-doped IST (Y-IST) are well matched with the calculated results of density functional theory (DFT). Set/reset speed of the Y-IST phase-change memory is faster than IST and $Ge_2Sb_2Te_5$ (GST) devices, which is strongly related with the fast and stable phase transition due to the larger lattice distortion. The power consumption of the Y-IST device is also less than a fourth of that of the GST device.

Recently, phase-change memory has been intensively investigated for non-volatile memory and neuromorphic systems with huge potential.[1–4] Typically, the phase-change material is a core for non-volatile phase-change random access memory (PRAM) and bio-inspired systems.[5–9] Faster speed and lower power consumption are directly related with the faster phase transition and lower melting temperature of the thermally stable ternary or quaternary materials since the repeated phase change between crystalline and amorphous states in thermodynamically unstable material will lead to the phase separation and the segregation.[10,11] So far, large number of research efforts have been devoted to dominantly, $Ge_2Sb_2Te_5$ (GST) and alternative materials such as In_3SbTe_2 (IST), Sb_3Te, and GeTe for improving the material characteristics and electrical performances by changing stoichiometry and doping method.[12–17]

M. Choi, S. Kwon, Prof. J. Ahn
Division of Materials Science and Engineering, Hanyang University, Seoul 04763, Korea jhahn@hanyang.ac.kr

Dr. H. Choi
Center of Materials Simulation Research, Virtual Lab Inc., Seoul 02792, Korea

Dr. H. Choi, Dr. S. Kim, Dr. K.-R. Lee
Center for Computational Science, Korea Institute of Science and Technology, Seoul 02792, Korea
E-mail: sckim@kist.re.kr

Prof. Y.T. Kim
Semiconductor Materials and Device Laboratory, Korea Institute of Science and Technology, Seoul 02792, Korea ytkim@kist.re.kr

Minho Choi and Heechae Choi contributed equally.

DOI: 10.1002/pssr.201700275

In this work, we have investigated the relationships among the dopant, the phase transition and the electrical properties using IST as a starting material because previous work preliminary suggested that the Bi dopant generated a lattice distortion and the set speed was improved by the Bi dopant.[18] However, there are still unknown facts: which element is the most proper dopant for IST and what relationships exist among the dopant, the lattice distortion, fast phase transition, and low power consumption. Therefore, a computational high-throughput screening of doping elements in the periodic table by density-functional theory (DFT) calculations is proposed for selecting an ideal one to satisfy the pre-determined criteria: (i) the element is doped into the IST with thermodynamic stability, and (ii) the element offers largest lattice distortion after the substitutional doping. After preparing the material doped with an ideal dopant, the atomic lattice structure, the phase transition process, and electrical performances of the prepared material have been thoroughly investigated with high-resolution transmission electron microscopy (HRTEM), and electrical measurements.

Among so many candidates from the periodic table, 29 dopants are chosen because some elements have been used as dopant and semiconductor. For example, a toxic element, Tl is used as $TlGaSe_2$ and considering the ionic radius difference with the host ion to investigate the relationship between lattice distortion and substitutional atoms. The computational dopant screening process selects limited number of elements and calculates the thermodynamic stability of the substitutional dopant with formation energy calculation using following Eq. (1):

$$\Delta E_f = E_{\mathrm{IST:D}} - E_{\mathrm{IST}} - E_{\mathrm{D}} + E_0, \quad (1)$$

where $E_{\mathrm{IST:D}}$, E_{IST}, E_{D}, and E_0 are, respectively, the calculated total energy of the doped IST, pure IST supercells, pure solid dopant, and pure solid of the removed host ion.

Figure 1(a) shows the doping formation energy of each element substituted into In, Sb, and Te sites, respectively in the atomic structure of IST. The energy indicates the stability of 29 dopants when the dopant occupies a host site among the In, the Sb, and the Te sites. Only four elements (Y, Gd, Bi, and La) represented by colored points have negative values of the doping formation, which means that these four elements can be the

© 2017 WILEY-VCH Verlag GmbH & Co. KGaA, Weinheim

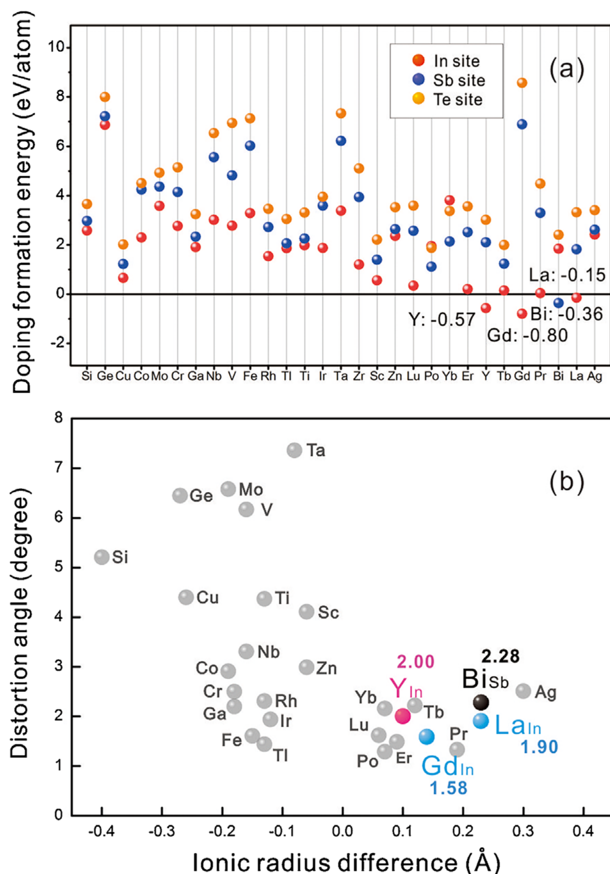

Figure 1. (a) Calculated doping formation energy corresponding to each of 29 elements substituted into the In (red color), Sb (blue color), and Te (yellow color) sites, respectively. (b) The distortion angle vs. the ionic radius difference ($R_d - R_h$) between the dopant (R_d) and the host ion (R_h).

adequate candidates with thermodynamic stability. The second criterion is to find the largest angular distortion generated by the dopant. Figure 1(b) shows the distortion angle calculated with DFT corresponding to ionic radius difference between the doping ion and the host ion. When the ionic radius of the dopant is relatively smaller than that of the host, the difference will be a negative value and the distortion angle becomes larger. This plotting trend can be explained with the tolerance factor,[26] meaning that if the host atoms are substituted by dopants with smaller ionic radius, the dopants prefer shorter bonding with neighborhood system, causing the asymmetric lattice distortion due to the asymmetric bond lengths.

Figure 1(a) and (b) clearly indicate that among 29 dopants, Y is the most proper dopant to satisfy the two criterions since the Y substitutes the In site with negative formation energy and has the largest distortion angle among the four candidates that have negative formation energy.

To confirm the dynamic motions of the IST and the Y-IST lattices at high temperature ($T = 1200$ K) by directly observing the amorphization process from crystalline state, ab initio molecular dynamics (AIMD) simulations of the IST and the Y-IST supercells are performed as shown in **Figure 2**. The

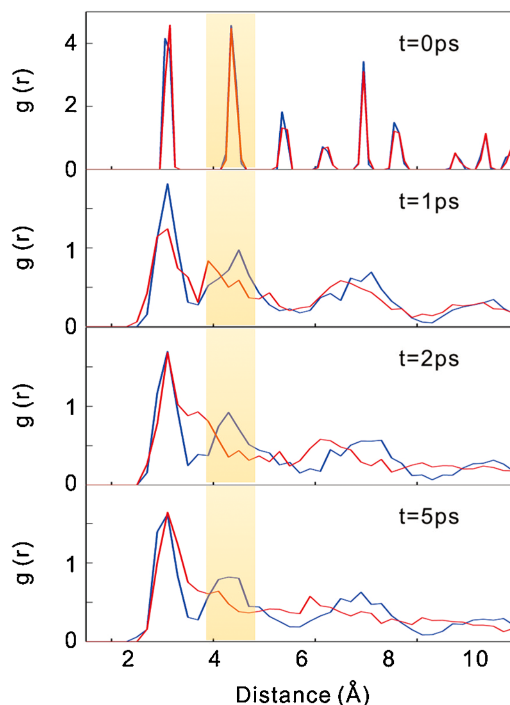

Figure 2. Radial distribution function of the IST (blue line) and the Y-IST (red line) supercells calculated by AIMD at 1200 K with time evolution from $t = 0$ to 5 ps. The peaks in the yellow-shaded range represent the 2nd nearest neighbor ions distribution in the IST and the Y-IST structures.

simulation result is the radial distribution function (RDF), $g(\mathbf{r})$ calculated for the IST and the Y-IST supercells by

$$g(\mathbf{r}) = \frac{1}{N\rho} \sum_{i=1}^{N} \sum_{k \neq i}^{N} [\delta(\mathbf{r} - \mathbf{r}_k - \mathbf{r}_i)], \tag{2}$$

where N, ρ, and $\mathbf{r}$ are the number of ions, density, and positions of ions, respectively, and i, k denote arbitrary positions of ions. In Figure 2, the second nearest neighbor (2NN) peaks in the yellow shaded region reveal that the 2NN position is seriously changed at the high temperature during the time evolution. The 2NN peak of the Y-IST presented by red line seems to be seriously collapsed compared with the blue line representing the 2NN peaks of the IST during $\Delta t = 5$ ps. This AIMD simulation obviously show that the amorphization of the IST lattice is accelerated by the Y dopant.

Interestingly, the calculated energy difference between the amorphous and the crystalline IST is 0.26 eV atom^{-1} and that of the Y-IST is 0.18 eV atom^{-1}. This means that the energy required for the amorphization of the Y-IST becomes lower than that of the IST by 0.08 eV atom^{-1}. Using the Arrhenius plot, $k(T) \propto \exp(-\Delta E/k_B T)$, where $k(T)$ is the rate constant depending on thermodynamic temperature, ΔE is the energy difference and k_B is the Boltzmann constant, it implies that the probability of the amorphization of the Y-IST is increased by the factor of 2.83 at usual operation temperature, $T = 900$ K. The DFT calculation and AIMD simulation suggest the phase transition of the Y-IST can be faster than that of the IST with thermodynamic stability and the origin of the fast and stable phase transition is due to the

© 2017 WILEY-VCH Verlag GmbH & Co. KGaA, Weinheim

larger distortion in the atomic structure of the Y-IST. Therefore, we have to confirm experimental results related with the crystalline structures, phase transition temperatures, and electrical properties of the Y-IST, IST, and GST thin films and the PRAM cell devices.

HRTEM images of the Y-IST are analyzed to observe the local distortion caused by the Y doping in the real atomic structure as shown in **Figure 3**(a)–(d). The atomic structure of IST is perfect NaCl-type structure and the inter-planar angles (θ_a, θ_b, θ_c, and θ_d) are 54.74°, 35.26°, 45°, and 45°, respectively.[27] The angular difference between the inter-planar angles of the IST and the distorted Y-IST is in the range from 0.25° to 1.98°, indicating that the maximum angular distortion ($\Delta\theta_{max}$) by the Y atom is 1.98°. This angular difference is observed from the inter-planar angle ($\theta_a + \Delta\theta$) between ($\bar{1}1\bar{1}$) and ($02\bar{2}$) in Figure 3(a), which is fairly well matched with 2.00° the distortion angle of Y_{In} calculated by DFT of 64 atoms supercell in the Figure 1(b), which is very similar to the maximum distortion angle (2.05°) calculated with the Y dopant in the 216-atom supercell. To confirm that the Y dopant substitutes the In site in the IST, the Y-IST and the Y thin films are annealed at 450 °C in the oxygen ambient.

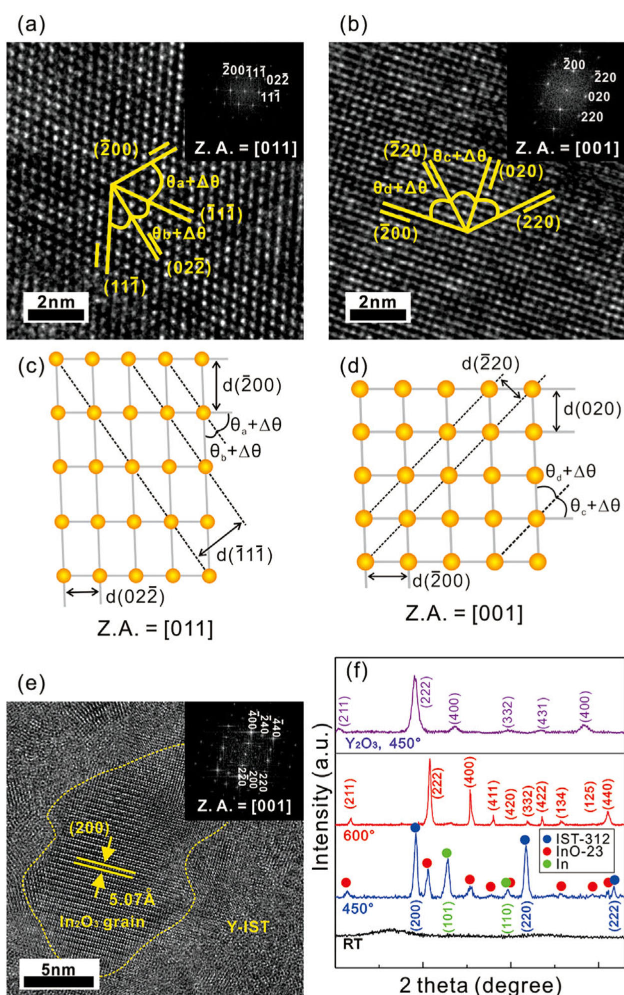

Figure 3. HRTEM images of Y-IST thin film along (a) the [011] zone axis and (b) [001] zone axis. Atomic lattice models distorted by Y atoms are shown on (c) [011] and (d) [001] zone axes. θ_a, θ_b, θ_c, and θ_d are the inter-planar angles of IST, $\Delta\theta$ is the angular difference due to the distortion by Y dopant in the atomic structure of Y-IST. (e) In_2O_3 grain in the Y-IST. (f) XRD patterns of the Y-IST thin film (room temperature (RT), 450 °C, and 600 °C) and annealed Y thin film (450 °C).

Figure 3(e) shows that a grain of In_2O_3 (JCPDS No. 65-3170) exists in the Y-IST thin film. It is well known that the In atom itself in the IST structure does not react with oxygen, but the In removed by the Y dopant can react with oxygen. X-ray diffraction (XRD) patterns of the Y-IST before and after oxidation show that the peaks of In (JCPDS No. 05-0642) and In_2O_3 are appeared with the peak of the IST phase, but Y_2O_3 peak is not observed in Figure 3(f). This means that the In removed by the substitutional Y in IST forms In_2O_3 by reacting with oxygen at 450 °C, and the Y atom in the IST does not form the Y_2O_3. However, the annealed Y in the Y thin film reacts with oxygen and forms the Y_2O_3 at the same condition as shown in the top pattern of Figure 3(f). It is confirmed that the Y substitutes the In site, resulting in large distortion in the Y-IST lattice structure.

Electrical characteristics of PRAMs fabricated with the Y-IST, IST and GST are shown in **Figure 4**. The set operations are measured at 2 V with variation of set pulse width from 60 to 250 ns by 10 ns intervals. Threshold voltages of Y-IST, IST, and GST are 1.83, 1.95, and 1.91 V, respectively. The Y-IST shows that the resistance starts to sharply drop at near 100 ns, the set point which means that the amorphous Y-IST begins to be crystalline state. Comparing with set speed of the IST presented in blue line, the set pulse width of the Y-IST is reduced from 220 to 100 ns, meaning that the set speed is over twice as fast. The set speed of the Y-IST is faster than that of the GST and the resistance difference between the amorphous and the crystalline states is wider than that of the GST, resulting in enough margin to operate with multi-level cell. Furthermore, this result is strongly related with the crystallization temperature. According to sheet resistance result as shown in the inserted figure, the crystallization temperature of the Y-IST is about 255 °C and that of the IST is 300 °C, which means that the fast set speed of the Y-IST is due to the fast transition at the relatively low crystallization temperature. In fact, the reset operation and the melting temperature are more important than the set and crystalline temperature.

The reset operations are obtained at 5 V reset bias with the reset pulse width from 60 to 300 ns by 10 ns intervals. The changing trend of the resistance curve of the Y-IST seems to be sharp compared with the gentle curvature of the IST and the GST PRAMs because the marked points represent the phase transition point from the crystalline to the fully amorphous state. The reset pulse width of the Y-IST is fairly well reduced to 90 ns comparing 165 ns, 230 ns of the GST and the IST PRAMs, respectively. This means that the reset speed of the Y-IST is faster than the IST and the GST, which is already predicted by the AIMD simulation and closely related with the fast and stable phase transition due to larger lattice distortion. From differential scanning calorimetry (DSC) measurements, the melting temperatures of the Y-IST (595 °C), the IST (634 °C[18]), and the GST (616 °C[28]) also support this result. The important fact is that the fast reset speed and high resistance value provide lower power consumption since the power consumption is proportional to reset pulse width and reversely with the resistance. The

© 2017 WILEY-VCH Verlag GmbH & Co. KGaA, Weinheim

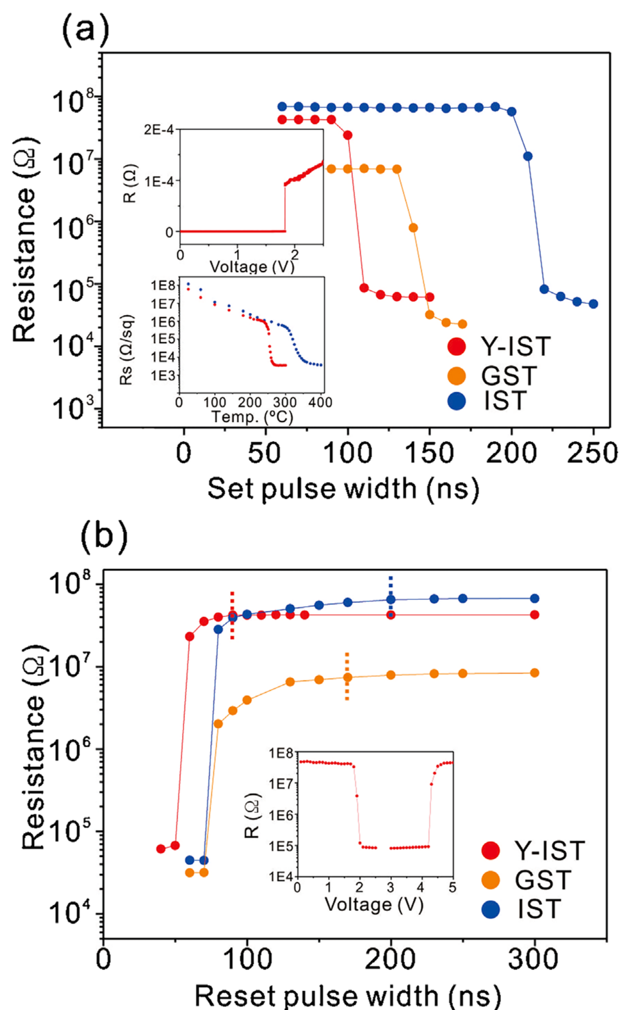

Figure 4. (a) Set and (b) reset characteristics of the Y-IST, IST, and GST PRAMs. Inserted figures in (a) are the *I–V* curve of Y-IST, and the sheet resistances of Y-IST and IST as a function of temperature. Inserted figure in (b) is *R–V* curve at fixed 100 ns width pulse.

measurement results clearly reveal that the joule energy for reset operation of the Y-IST PRAM is 52.8 pJ (371 μW), which is quite lower than 155 pJ (549 μW) and 227 pJ (901 μW) of the IST and the GST PRAMs, respectively.

In conclusion, to optimize relationship between the distortion and dopants with lower power consumption, the thermal and electrical properties of IST phase-change material have been investigated. A computational high-throughput screening method has been used for selecting an adequate dopant element and material,[29,30] and the Y has been identified as a suitable dopant for the IST because of its negative doping formation energy and large distortion angle. AIMD predicts the stable and fast phase transition of the Y-IST due to lower energy difference between amorphous and crystalline state. Experimentally, the atomic lattice structures clearly show that larger lattice distortion is originated by the substitutional Y dopant. The set/reset characteristics and crystallization/melting temperatures of the Y-IST, IST, and GST clearly indicate that the phase transition of the Y-IST is faster than the IST and the GST and the power consumption is also obviously reduced by the Y dopant. This result will be useful for modifying the IST by using the dopant and designing the fast and low-power applications with good stability.

Experimental Section

The Y-doped IST thin films are co-sputtered with yttrium and In_3SbTe_2 targets. The composition of sputtered Y-IST is $Y_{12.38}(In_3SbTe_2)_{87.62}$. Devices of IST and GST are sputtered by single targets of In_3SbTe_2 and $Ge_2Sb_2Te_5$, respectively. The sputtering process are conducted at room temperature in an Ar atmosphere. The PRAM devices are fabricated with cell size of $250 \times 250\,nm^2$. The cross sectional structure is consisted of TiN (bottom electrode)/phase-change material/TiN/Ti (top electrode) and the thickness of phase-change material is 100 nm. The electrical characteristics are measured with both of Keithley 4200-SCS semiconductor characterization system, Keithley 4225-PMU ultra-fast *I–V* module, Keithley 4225-RPM remote amplifier/switch, and Keithley 3402 pulse/pattern generator. HRTEM analysis was conducted using FEI TITAN at 300kV. The fast Fourier transform (FFT) was obtained by Gatan Digital Micrograph. The samples were annealed by rapid thermal annealing (RTA) process at 450 °C for 30 min and prepared by mechanical polishing. The diffraction patterns of annealed thin films were also obtained with X-ray diffractometer.

DFT[19,20] calculations are performed with the Vienna ab initio simulation package (VASP) program using the generalized gradient approximation (GGA) and Perdew-Burke-Ernzerhof (PBE) parameterization.[21,22] In these DFT calculations, Kohn-Sham orbitals are expanded with a cut-off energy of 400.0 eV, and $2 \times 2 \times 2$ equally spaced k-point grids are used for the Brillouin zone sampling.[23] The supercell volume and all atoms are fully relaxed. The dimension of IST supercell is fixed at 12.435 Å and the time step of AIMD is 1 fs. In previous DFT studies, employing a 216-atom IST supercell was useful for understanding the chemical bonding nature of stoichiometric IST.[24,25] In this work, we have used a 64 atom IST supercells model instead of 216 atoms because it shortens the time cost for high throughput screening and it is enough for understanding the local lattice distortion without considering the spurious defect–defect interactions with large scale atoms. However, to valid 64-atom supercell model, we have also cross checked the Y-induced lattice distortion by using a 216-atom IST supercell with a dimension of 18.72 Å under the condition that in the pure IST supercell without lattice distortion, the Y composition is fixed at 5% of In-site, 11 In-atoms are substituted with Y dopant.

Acknowledgements

This research was supported by Ministry of Science, ICT and Future Planning under the Grant No. 2U06100 "Extremely low power consumption technology of eDRAM for Internet of Things", Nano · Material Technology Development Program (2015M3A7B7045353) through the National Research Foundation of Korea (NRF) funded by the Ministry of Science, ICT and Future Planning, and Grant No. 2016M3A7B4024131 funded by Ministry of Science, ICT and Future planning.

© 2017 WILEY-VCH Verlag GmbH & Co. KGaA, Weinheim

Conflict of Interest

The authors declare no conflict of interest.

Keywords

distortion, doping, In_3SbTe_2, phase change materials, phase change memory

Received: August 15, 2017
Revised: September 8, 2017
Published online: September 20, 2017

[1] C. D. Wright, P. Hosseini, J. A. V. Diosdado, *Adv. Funct. Mater.* **2013**, *23*, 2248.
[2] B. Gao, Y. Bi, H.-Y. Chen, R. Liu, P. Huang, B. Chen, L. Liu, X. Liu, S. Yu, H.-S. P. Wong, *ACS Nano* **2014**, *8*, 6998.
[3] S. Raoux, F. Xiong, M. Wuttig, E. Pop, *MRS Bull.* **2014**, *39*, 703.
[4] S. Ambrogio, N. Ciocchini, M. Laudato, V. Milo, A. Pirovano, P. Fantini, D. Ielmini, *Front. Neurosci.* **2016**, *10*, 56.
[5] T. H. Lee, D. Loke, K. J. Huang, W. J. Wang, S. R. Elliott, *Adv. Mater.* **2014**, *26*, 7493.
[6] C. D. Wright, Y. Liu, K. I. Kohary, M. M. Aziz, R. J. Hicken, *Adv. Mater.* **2011**, *23*, 3408.
[7] M. Suri, O. Bichler, D. Querlioz, O. Cueto, L. Perniola, V. Sousa, D. Vuillaume, C. Gamrat, B. DeSalvo, 2011 IEEE International Electron Devices Meeting (IEDM),Washington D.C. **2011**.
[8] G. W. Burr, B. N. Kurdi, J. C. Scott, C. H. Lam, K. Gopalakrishnan, R. S. Shenoy, *IBM J. Res. Dev.* **2008**, *52*, 449.
[9] D. Kuzum, R. G. Jeyasingh, B. Lee, H.-S. P. Wong, *Nano Lett.* **2011**, *12*, 2179.
[10] C. Kim, D. Kang, T.-Y. Lee, K. H. Kim, Y.-S. Kang, *Appl. Phys. Lett.* **2009**, *94*, 193504.
[11] S. Raoux, R. M. Shelby, J. Jordan-Sweet, B. Munoz, M. Salinga, Y.-C. Chen, Y.-H. Shih, E.-K. Lai, M.-H. Lee, *Microelectron. Eng.* **2008**, *85*, 2330.
[12] J. Orava, A. Greer, B. Gholipour, D. Hewak, C. Smith, *Nat. Mater.* **2012**, *11*, 279.
[13] G. Wang, Q. Nie, X. Shen, R. Wang, L. Wu, J. Fu, T. Xu, S. Dai, *Appl. Phys. Lett.* **2012**, *101*, 051906.
[14] R. Fallica, E. Varesi, L. Fumagalli, S. Spadoni, M. Longo, C. Wiemer, *Phys. Status Solidi RRL* **2013**, *7*, 1107.
[15] X. Ji, L. Wu, W. Zhou, M. Zhu, F. Rao, Z. Song, L. Cao, S. Feng, *Appl. Phys. Lett.* **2015**, *106*, 023118.
[16] S. K. Pandey, A. Manivannan, *Appl. Phys. Lett.* **2016**, *108*, 233501.
[17] T. Schröder, T. Rosenthal, S. Grott, C. Stiewe, J. de Boor, O. Oeckler, *Z. Anorg. Allg. Chem.* **2013**, *639*, 2536.
[18] M. Choi, H. Choi, S. Kim, J. Ahn, Y. T. Kim, *Sci. Rep.* **2015**, *5*, 12867.
[19] W. Kohn, L. J. Sham, *Phys. Rev.* **1965**, *140*, A1133.
[20] J. Ihm, A. Zunger, M. L. Cohen, *J. Phys. C: Solid State Phys.* **1979**, *12*, 4409.
[21] J. P. Perdew, J. Chevary, S. Vosko, K. A. Jackson, M. R. Pederson, D. Singh, C. Fiolhais, *Phys. Rev. B* **1992**, *46*, 6671.
[22] J. P. Perdew, K. Burke, M. Ernzerhof, *Phys. Rev. Lett.* **1996**, *77*, 3865.
[23] H. J. Monkhorst, J. D. Pack, *Phys. Rev. B* **1976**, *13*, 5188.
[24] V. L. Deringer, W. Zhang, P. Rausch, R. Mazzarello, R. Dronskowski, M. Wuttig, *J. Mater. Chem. C* **2015**, *3*, 9519.
[25] J. H. Los, T. D. Kühne, S. Gabardi, M. Bernasconi, *Phys. Rev. B* **2013**, *88*, 174203.
[26] K. Singh, S. Acharya, D. Atkare, *Ferroelectrics* **2005**, *315*, 91.
[27] C. S. Kim, J. Y. Lee, Y. T. Kim, *Appl. Phys. Lett.* **2012**, *100*, 151903.
[28] N. Yamada, E. Ohno, K. Nishiuchi, N. Akahira, M. Takao, *J. Appl. Phys.* **1991**, *69*, 2849.
[29] R. Armiento, B. Kozinsky, M. Fornari, G. Ceder, *Phys. Rev. B* **2011**, *84*, 014103.
[30] J. Greeley, T. F. Jaramillo, J. Bonde, I. Chorkendorff, J. K. Nørskov, *Nat. Mater.* **2006**, *5*, 909.

© 2017 WILEY-VCH Verlag GmbH & Co. KGaA, Weinheim